 doi:10.20944/preprints202206.0222.v1

Article

Dynamic Reduction-based Virtual Models for Digital Twins-A Comparative Study

Soumya Maulik [1,2,3,4]*, Daniel Riordan [1,2,3,4] and Joseph Walsh [1,2,3,4]

[1] IMaR Research Centre, Munster Technological University, V92 CX88 Tralee, Ireland 1; Joseph.Walsh@mtu.ie
[2] School of Science Technology, Engineering and Mathematics, Munster Technological University, V92 CX88 Tralee, Ireland; Joseph.Walsh@mtu.ie
[3] Department of Technology, Engineering, and Mathematics, Munster Technological University, V92 CX88 Tralee, Ireland; Daniel.Riordan@mtu.ie
[4] Lero—Science Foundation Ireland Research Centre for Software, V92 NYD3 Limerick, Ireland; Joseph.Walsh@mtu.ie
* Correspondence: Soumya.Maulik@research.ittralee.ie

Abstract: Digital models are the foundation of digital twins, which form the basis of autonomous off-road vehicles. Developing virtual models of off-road vehicles using dynamic reduction techniques is one of several approaches. The article commences with a comprehensive overview of the most widely used dynamic reduction methods and then introduces performance metrics for assessing their efficacies in the context of digital twins. The paper additionally includes a detailed mathematical derivation of the state-space representation for reduced-order finite element models. The state-space representation of the reduced finite element models facilitates their export to problem-solving environments for dynamic analysis. The state-space models are eventually solved utilizing the built-in libraries of numerical solvers in textual and graphical programming platforms. In addition, the article identifies the set of solvers that best suit the simulation of virtual models for off-road vehicles. This article also includes an evaluation of the simulation results for digital models with modes ranging from 0 to 30 Hz. In addition, the article demonstrates the lower bound of the frequency range necessary and sufficient to be retained in off-road vehicle virtual models. Finally, the paper presents the simulation outcomes for digital models of commercial off-road vehicles with custom-built powertrain, electrical, and control systems.

Keywords: digital twin; Industry 4.0; MATLAB; ANSYS; simulation; crane; modal analysis; dynamic substructuring; dynamic reduction; component modal synthesis

List of Symbols

$[\bar{\phi}_n]$	Matrix of retained fixed-constraint normal modeshapes
$[\bar{\phi}_{Bn}]$	Matrix of retained free-interface modeshapes corresponding to boundary degrees of freedom
$[\bar{\phi}_{In}]$	Matrix of retained free-interface modeshapes corresponding to interior degrees of freedom
$[\bar{C}]$	Boolean matrix
$[\bar{k}]$	Stiffness Matrix in generalized coordinates
$[\bar{m}]$	Mass Matrix in generalized coordinates
$[\beta]$	Compatibility matrix
$[\beta^p]$	Boolean matrix
$[\phi]$	Matrix of modeshapes for the reduced-order model

 doi:10.20944/preprints202206.0222.v1

$[\phi^{ss}]$	Modified modeshape matrix of reduced system
$[\phi_a]$	Matrix of retained attachment modeshapes
$[\phi_c]$	Matrix of constraint modeshapes
$[\phi_e]$	Matrix of elastic modeshapes
$[\phi_n]$	Matrix of fixed-constraint normal modeshapes
$[\phi_o]$	Matrix of rigid body modeshapes
$[\Psi]$	Inertia-relief matrix
$[A]$	State matrix
$[B]$	Input matrix
$[C]$	Output matrix
$[D]$	Feed-forward matrix
$[k]_i$	Stiffness Matrix of the ith substructure in physical coordinates
$[K_r]$	Reduced stiffness matrix in physical coordinates
$[m]_i$	Mass Matrix of the ith substructure in physical coordinates
$[M_r]$	Reduced mass matrix in physical coordinates
$[T_{CB}]$	Craig-Bampton transformation matrix
$[T_H]$	Hintz's transformation matrix
ϵ_i	Percentage error between ith reduced-order and full-order mode
ω	Natural frequencies of full-order system
$\Omega(t_i^d)$	Reference trajectory at time t_i^d in the deceleration regime, and where t_0^d indicates the beginning of the braking of regime
$\Omega(t_i^{as})$	Reference trajectory at time t_i^{as} in the acceleration and steady state regime, and where t_0^{as} indicates the vehicle is commencing travel
ω_*	Retained modes in reduced system
ω_n	Fixed-constraint normal modes
Ω_r	Electrical machine rated speed
ω_{fn}	Free-interface normal modes
τ	Total number of substructures or components
τ_c	Total number of couplings in the structure
Θ_a	A constant and $\Theta_a > 0$
Θ_d	A constant and $\Theta_d < 0$
$\{\bar{u}\}$	Global physical displacements
$\{\bar{u}_B\}$	Global physical displacements for uncoupled boundary coordinates
$\{\ddot{u}\}$	Local acceleration in physical coordinates
$\{\eta\}$	Modal coordinates

 doi:10.20944/preprints202206.0222.v1

$\{\eta_r\}$	Modal coordinates for reduced-order model
$\{\mu\}$	Generalized coordinates
$\{\phi_B\}$	Eigenvectors of free-interface modes corresponding to boundary degrees of freedom
$\{\phi_I\}$	Eigenvectors of free-interface modes corresponding to interior degrees of freedom
$\{p\}$	External forces in physical coordinates
$\{p_o\}$	D'Alembert's forces or inertial forces
$\{p_r\}$	External force at the rth degree of freedom of the reduced-order model
$\{u\}$	Local displacements in physical coordinates
$\{u_e\}$	Elastic deformation vector
$\{u_o\}$	Rigid body displacement
$\{x\}$	State variables
$\{z\}$	Input vector
B	Boundary degrees of freedom in ith substructure
h	Simulation step size
I	Interior degrees of freedom in ith substructure
N	Total degrees of freedom in full-order system
N_i^I	Total degrees of freedom for ith substructure
R	Retained degrees of freedom in reduced system
s_d	Distance to be traveled
s_i	Displacement of the vehicle at time t_i^{as} or t_i^d
s_N	Displacement at the narrow side
s_W	Displacement at the wide side
t	Simulation epoch
v_i	Velocity of the vehicle at time t_i^{as} or t_i^d
v_m	Maximum allowable velocity for the off-road vehicle

1. Introduction

The technical cornerstone of Industry 4.0 [1–19] is the Internet of Things (IoT) [20,21], which envisions integrating electronics, software, sensors, and network connectivity into devices to facilitate the seamless transfer of data over the internet. The introduction of IPV6 [22,23], the availability of affordable sensors, and the enhancement of computing hardware have eased data acquisition and processing of sensory information. Consequently, data-driven decision-making and device management in the industrial environment are now more practically feasible than before. The decision-making and control of operating structures can be accomplished by comparing the pooled data from the sensors installed on them with the simulated output of their digital equivalents, a concept referred to as a "digital twin" [24–50], which is also one of the theoretical frameworks associated with the Industry 4.0 revolution. The use of digital twins for aviation prognostics and diagnostics operations has yielded considerable benefits for aerospace and space organizations. In the

 doi:10.20944/preprints202206.0222.v1

realm of the aerospace industry, NASA's initial definition of a digital twin was "an integrated multi-physics, multi-scale, probabilistic simulation of a vehicle or system that uses the best available physical models, sensor updates, fleet history, etc., to mirror the life of its flying twin. The digital twin is ultra-realistic and may consider one or more important and interdependent vehicle systems" [51]. As stated in the definition, the primary objective of a digital twin is to replicate the life of an aircraft in cyberspace using the "best" physics-based digital model that consists of the integration of sub-components that represent the overall structure. While the aerospace industry and space agencies, in particular, have reaped immense benefits, the adoption of digital twins for heavy off-road vehicles is rare. There are potential benefits of digital twin models for the latter sector, including but not limited to enhanced operational efficiency, improved maintenance regimes that can prevent expensive faults, optimized asset utilization, reduced operating expenses, and remote commissioning. A virtual model that encompasses the entire set of coordinates of a full-order model for a structure accurately and consistently represents the deformed shape, but it requires solving large matrices. Consequently, simulation of virtual models with the entire set of principal coordinates is computationally expensive and has a prolonged runtime, preventing real-time synchronization with the activities of their physical counterparts operating in an industrial environment. This article proposes dynamic reduction-based virtual models as a solution to these challenges.

Dynamic reduction techniques came into existence from 1960 onwards and are referred to as "component modal synthesis" in the field of structural dynamics [52,53], and "substructuring" in statics [54], with the original objectives of (i) minimizing the computational cost of analysis of structures with a large number of degrees of freedom and (ii) analyzing constituent substructures of a structure independently in such a manner that it would be feasible to amalgamate the results. Nonetheless, dynamic model reduction schemes have the potential to make a substantial contribution to the development of physics-based virtual models.

Substructure coupling approaches may be primarily categorized based on the types of modes employed for modeling the reduced finite element representation of a component as

1. Fixed-Interface methods [55–57]
2. Free-Interface methods [58–61]
3. Loaded-Interface [62], and,
4. Hybrid methods [63,64]

The substructure interfaces in fixed-interface schemes are entirely constrained, whereas the substructure interfaces in free-interface methods are unrestricted. The "loaded-interface" methods, which augment the interface loading components in the structural matrices of the substructures, are related to the free-interface schemes. Hybrid techniques allow for arbitrary restrictions at substructure boundaries, and in the most generalized situation, these constraints can be a combination of the three types of outlined coupling methods. The fundamental objective of this research is to identify the high-fidelity dynamic model reduction approach that "best" suits the development of digital models for off-road vehicles from among those that are typically accessible as built-in libraries in commercial FEA-based modeling platforms. In this article, Craig-Bampton and Hintz's modal synthesis techniques for fixed-interface and free-interface methods, respectively, are considered.

In addition to reduced structural models, digital models for off-road vehicles comprise virtual models of driveline systems, electrical components, and powertrain control modules. Textual and graphical programming platforms, unlike FEA-based platforms, use uncluttered programming syntax and are thus deemed appropriate for the design, modeling, and simulation of specialized powertrain, electrical, and control systems. Finally, the state-space representation of reduced structural models can be incorporated into problem-solving environments and subsequently coupled with custom-built powertrain, electrical, and control systems to develop virtual models for off-vehicles in cyberspace.

The virtual models facilitate the yield of physics-based digital twins for off-road vehicles; however, there is hardly any extant literature presenting their development methods. This

 doi:10.20944/preprints202206.0222.v1

paper proposes dynamic reduction methods for developing reduced-order models that subsequently represent the virtual models for off-road vehicles. Simulation of these digital models with reduced degrees of freedom improves speed without impacting accuracy. Furthermore, built-in packages of FEA-based software, predominately used for structural modeling and analysis, incorporate these high-fidelity dynamic reduction techniques, thereby enabling the development of the reduced-order models on the same platforms where designed. This article outlines the state-space representation method for these reduced-order models. The state-space models facilitate the simulation of reduced-order models in problem-solving environments. This paper, in addition, provides a comprehensive mathematical derivation for the state-space representation of reduced-order models. To accomplish real-time synchronization with the activities of a physical counterpart in an industrial environment, the simulation time of virtual models must be less than or equal to the operating time of physical equivalents. As a result, a comparative analysis of the execution times in a problem-solving environment of digital models developed utilizing Craig-Bampton and Hintz's component modal synthesis is provided. It is worth noting that these virtual models are eventually solved utilizing solvers that are available as built-in libraries on textual and graphical programming platforms; hence, selecting the optimal solver among the available solvers is critical. Consequently, this paper presents a comparative assessment of the execution times of virtual models for off-road vehicles employing these solvers.

The remainder of this article is structured as follows: Section 2 presents a comprehensive review of the dynamic reduction techniques and the state-space representation of the reduced finite-element model. Section 3 outlines the metrics for evaluating the dynamic reduction methods. Section 4 presents the results, and finally, Section 5 concludes the article.

2. Component Modal Synthesis

The superposition of principal modes, also referred to as the normal mode method [65], is a fundamental and extensively used analytical approach for solving vibration problems. In this method, linear transformations in terms of modal vectors, in conjunction with the orthogonality of modal vectors, enable the transformation of a set of simultaneous equations of motion in physical coordinates into a set of independent modal equations. For large and complex industrial structures, an eigensolution, which is the most fundamental part of a dynamic analysis using the normal mode method, becomes uneconomical due to the sheer number of equations of motion. Dynamic reduction methods alleviate the computational constraints of dealing with large matrices by obtaining the principal modes of the overall system from parts rather than as a whole. In these methods, multiple eigenvalue problems involving individual constituent components represented by smaller matrices are used rather than a single eigenvalue problem representing the entire structure. The coordinate system obtained by synthesizing the components is assembled for system synthesis, yielding one final eigenvalue problem, typically of smaller size.

A substructure, in general, contains a set of constraints at its interfaces coupled with neighboring substructures. General displacement within a substructure is defined in dynamic reduction methods by superimposing displacements relative to component boundaries, from which a set of generalized coordinates applicable to the entire structure is synthesized. One of the subcategories of dynamic reduction methods is fixed-interface component modal synthesis. The fixed-interface component modal synthesis by Craig-Bampton is one of the most widely used dynamic reduction techniques, and most FEA-based systems have built-in libraries, as outlined in the following section.

2.1. Fixed-Interface Modal Synthesis Technique

Hurty pioneered the notion of fixed-interface component modal synthesis [56], but the method was incompatible with automation. Craig-Bampton [57] modified Hurty's approach, removing the limitations that facilitated the implementation of the modal synthesis process on computing platforms. Craig-Bampton's method analyzes components by the

Preprints (www.preprints.org) | NOT PEER-REVIEWED | Posted: 15 June 2022 doi:10.20944/preprints202206.0222.v1

superimposition of constraint and fixed-constraint normal modes.
Constraint modes are the displacements of interior coordinates in a substructure induced by sequential unit displacements of interface constraints, with the remaining boundary constraints being constrained. The boundary constraints are usually imposed on the coupled points between interconnected substructures. These coupled points are subjected to unit displacement in the direction of each degree of freedom, considered one at a time, resulting in the deflection of the substructure. The deflected configurations of the substructure are the constraint modes for that individual substructure. For the ith substructure, the linear relationship between the externally applied force and stiffness for static analysis is given by

$$\left\{\begin{array}{c} p_B \\ \hdashline p_I \end{array}\right\}_i = \left[\begin{array}{c:c} k_{BB} & k_{BI} \\ \hdashline k_{BI}^{\mathsf{T}} & k_{II} \end{array}\right]_i \left\{\begin{array}{c} u_B \\ \hdashline u_I \end{array}\right\}_i \tag{1}$$

Because there is no external force acting on the unconstrained coordinates in constraint mode analysis, taking the bottom partition of Equation 1 yields

$$\begin{aligned} &[k_{BI}]_i^{\mathsf{T}}\{u_B\}_i + [k_{II}]_i\{u_I\}_i = \{0\} \\ &\{u_I\}_i = -[k_{II}]_i^{-1}[k_{BI}]_i^{\mathsf{T}}\{u_B\}_i = [\phi_c]_i\{u_B\}_i \end{aligned} \tag{2}$$

Fixed-constraint normal modes are defined by displacements of interior points in the component relative to the interface constraints. These are the normal modes of vibration with all interface constraints fixed, typically computed by eigenvalue analysis of the substructure. The zero-input response and eigenanalysis of a system are analogous, and therefore, in the absence of external excitation in the internal degrees of freedom, the undamped equation of motion for the ith substructure can be expressed as,

$$\begin{aligned} &\left[\begin{array}{c:c} m_{BB} & m_{BI} \\ \hdashline m_{BI}^{\mathsf{T}} & m_{II} \end{array}\right]_i \left\{\begin{array}{c} \ddot{u}_B \\ \hdashline \ddot{u}_I \end{array}\right\}_i \\ &+ \left[\begin{array}{c:c} k_{BB} & k_{BI} \\ \hdashline k_{BI}^{\mathsf{T}} & k_{II} \end{array}\right]_i \left\{\begin{array}{c} u_B \\ \hdashline u_I \end{array}\right\}_i = \left\{\begin{array}{c} p_B \\ \hdashline 0 \end{array}\right\}_i \end{aligned} \tag{3}$$

In fixed-interface normal mode analysis, the constraints on the interface coordinates for a substructure are constrained, resulting in

$$\{u_B\} = 0$$

and

$$\{\ddot{u}_B\} = 0 \tag{4}$$

Substituting Equation 4 into Equation 3 and using the lower partition yield

$$[m_{II}]_i\{\ddot{u}_I\}_i + [k_{II}]_i\{u_I\}_i = \{0\} \tag{5}$$

The free vibration solution for Equation 5 is of the form $\{u_I\}_i = [\phi_n]_i\{\eta_n\}_i$. Therefore, Equation 5 reduces to the eigenvalue problem

$$([k_{II}]_i - [\omega_n^2]_i[m_{II}]_i)\{\phi_I\}_i = 0$$

and

$$\left|[k_{II}]_i - [\omega_n^2]_i[m_{II}]_i\right| = 0 \tag{6}$$

where $[\omega_n^2]_i = diag(\omega_{n_1}^2, \ldots, \omega_{n_{N_i^I}}^2)$. The mass normalized eigenvectors form the respective columns of $[\phi_n]_i$ of the ith constrained substructure. The elements of $[\phi_n]_i$ to be retained are then collected in $[\bar{\phi}_n]_i$ and thereby retain the associated interior degrees of freedom of

Preprints (www.preprints.org) | NOT PEER-REVIEWED | Posted: 15 June 2022 doi:10.20944/preprints202206.0222.v1

the substructure. The interface coordinates being entirely constrained in fixed-constraint normal mode analysis renders the upper partition of Equation 3 redundant. It is worth mentioning that the constraint modes represent the static characteristics of the substructure, while the fixed constraint normal modes, as determined by vibration analysis, demonstrate the dynamic behavior of the substructure.
Finally, the transformation from physical coordinates to generalized coordinates for the ith substructure is then,

$$\begin{aligned}\{u\}_i &= \left[\begin{array}{c:c} I & 0 \\ \hdashline \phi_c & \bar{\phi}_n \end{array}\right]_i \left\{\begin{array}{c} u_B \\ \hdashline \eta_n \end{array}\right\}_i \\ &= [T_{CB}]_i \left\{\begin{array}{c} u_B \\ \hdashline \eta_n \end{array}\right\}_i \end{aligned} \tag{7}$$

It is worth noting that truncating the constraint modes isn't feasible since they characterize the entire motion of the system.
The reduced mass and stiffness matrix of the ith substructure in generalized coordinates is then expressed as

$$\begin{aligned}[\bar{m}]_i &= [T_{CB}]_i^{\mathsf{T}} [m]_i [T_{CB}]_i \\ [\bar{k}]_i &= [T_{CB}]_i^{\mathsf{T}} [k]_i [T_{CB}]_i \end{aligned} \tag{8}$$

The equations of motion for the overall structure in the unconnected form are eventually obtained by grouping together the equations of motion for all $\tau \in \mathbb{N}^+$ substructures. A compatibility matrix ($[\beta]$) renders constraints on the interconnected substructures, ensuring compatible displacements at substructure boundaries. The boundary coordinates for any two adjoining substructures i and j are expressed in their respective local coordinate frames of reference, $\{u\}_i$ and $\{u\}_j$, and consequently, it is imperative to express their frame of reference in a shared global reference frame, $\{\bar{u}\}$, prior to establishing compatible displacement connections. Let the boundary coordinates for the ith and jth substructures in the global frame of reference be $\{\bar{u}_B\}_i^s$ and $\{\bar{u}_B\}_j^s$, respectively, at a common connection point s. Then, the following necessary and sufficient conditions must be satisfied at the boundary to ensure that a substructure's displacements on its boundary correspond to those of its adjoining substructures in the global frame of reference:

$$\{\bar{u}_B\}_i^s = \{\bar{u}_B\}_j^s \tag{9}$$

For the sake of brevity, superscript (s) in Equation 9 will be omitted. In terms of interconnected substructures, there are no compatibility constraints for the modal coordinates. Furthermore, any arbitrary substructure i with multiple couplings to adjoining substructures may be expressed using a matrix notation $[\beta]_i$. Finally, the general form of the transformation of coordinates to represent the overall structure is as follows:

$$\begin{aligned}\begin{Bmatrix} u_{B_1} \\ \eta_{n_1} \\ \vdots \\ u_{B_\tau} \\ \eta_{n_\tau} \end{Bmatrix} &= \begin{bmatrix} \beta_1 \\ \vdots \\ \beta_\tau \end{bmatrix} \begin{Bmatrix} \bar{u}_{B_1} \\ \vdots \\ \bar{u}_{B_{\tau_c}} \\ \bar{u}_B \\ \eta_{n_1} \\ \vdots \\ \eta_{n_\tau} \end{Bmatrix} \\ &= [\beta]\{\mu\} \end{aligned} \tag{10}$$

Preprints (www.preprints.org) | NOT PEER-REVIEWED | Posted: 15 June 2022 doi:10.20944/preprints202206.0222.v1

The uncoupled set of boundary coordinates mentioned in Equation 10 is where external excitations are applied. Finally, the equation of motion for free vibration of the complete structure may be expressed as

$$[M_\mu]\{\ddot{\mu}\} + [K_\mu]\{\mu\} = 0 \tag{11}$$

where $[M_\mu] = [\beta]^\intercal[\bar{M}_\mu][\beta]$ and $[K_\mu] = [\beta]^\intercal[\bar{K}_\mu][\beta]$, and where

$$\bar{M}_\mu = \begin{bmatrix} [\bar{m}]_1 & & \\ & \ddots & \\ & & [\bar{m}]_\tau \end{bmatrix}, \quad \bar{K}_\mu = \begin{bmatrix} [\bar{k}]_1 & & \\ & \ddots & \\ & & [\bar{k}]_\tau \end{bmatrix}$$

The Craig-Bampton modal synthesis technique has a high degree of accuracy, and built-in libraries are usually available in most FEA-based software products [66–68].

2.2. Free-Interface Modal Synthesis Techniques

The presence of rigid body motion is one of the characteristics of free-free or unconstrained systems. For such systems, the stiffness matrix is singular, and hence no flexibility matrix exists, jeopardizing static analysis. In his modal synthesis approach, Hintz eliminated the rigid body modes using the inertia relief matrix, facilitating the analysis of the elastic behavior of such unconstrained systems. The free-interface modal synthesis scheme proposed by Hintz [61] for free-free systems constitutes attachment modes for unconstrained systems or inertia relief modes, constraint modes, and free-interface normal modes of substructures.

For the ith substructure the free-interface normal modes are obtained by setting Equation 3 for $\{p_B\} = 0$. By substituting $\{p_B\} = 0$, Equation 3 reduces to

$$\begin{aligned} &\left[\begin{array}{c:c} m_{BB} & m_{BI} \\ \hdashline m_{BI}^\intercal & m_{II} \end{array}\right]_i \left\{\begin{array}{c} \ddot{u}_B \\ \hdashline \ddot{u}_I \end{array}\right\}_i \\ &+ \left[\begin{array}{c:c} k_{BB} & k_{BI} \\ \hdashline k_{BI}^\intercal & k_{II} \end{array}\right]_i \left\{\begin{array}{c} u_B \\ \hdashline u_I \end{array}\right\}_i = \left\{\begin{array}{c} 0 \\ \hdashline 0 \end{array}\right\}_i \end{aligned} \tag{12}$$

Thus,

$$([k]_i - [\omega_{fn}^2]_i[m]_i)\left\{\begin{array}{c} \phi_B \\ \hdashline \phi_I \end{array}\right\}_i = \{0\}$$

and

$$\left|[k]_i - [\omega_{fn}^2]_i[m]_i\right| = 0 \tag{13}$$

where $[\omega_{fn}^2]_i = diag(\omega_{fn_1}^2, \ldots, \omega_{fn_{N_i}}^2)$.If the ith substructure is unrestrained, then rigid body modes are included in $[\omega_{fn}^2]_i$. The mass normalized eigenvectors corresponding to the free-interface normal modes belonging to the interior and boundary degrees of freedom for the ith substructure to be retained are gathered in $[\overline{\phi}_{In}]_i$ and $[\overline{\phi}_{Bn}]_i$, respectively, thereby retaining the corresponding coordinates. Furthermore, truncation of the free-normal modes renders elimination of the associated degrees of freedom.

Let W_i be the set of physical coordinates for the ith substructure, where $W_i \subset N_i \setminus O_i$, and where O_i is the statically determinate constraint set sufficient to provide restraint against rigid body motion. Furthermore, let us define a set such that $L_i \subset W_i$. The static deflection as a consequence of an applied unit force on $w_j^i \in W_i$, where $j \in \{1, \ldots, |W|\}$ while the remaining of the degrees of freedom in the set W_i are devoid of force, is characterized as the attachment mode.

Preprints (www.preprints.org) | NOT PEER-REVIEWED | Posted: 15 June 2022 doi:10.20944/preprints202206.0222.v1

Separating the displacement vector for the ith substructure into pure rigid body displacement $\{u_o\}$, and elastic deformation vector $\{u_e\}$ yields

$$\{u\}_i = \{u_o\}_i + \{u_e\}_i \tag{14}$$

The displacements in physical coordinates can be expressed in modal coordinates in the following way

$$\{u\}_i = \left[\begin{array}{c:c} \phi_o & \phi_e \end{array}\right]_i \left\{\begin{array}{c} \eta_o \\ \hdashline \eta_e \end{array}\right\}_i \tag{15}$$

Using the non-homogeneous undamped equation of motion and knowing that $[k]_i[\phi_o]_i = 0$, the modal coordinates associated with rigid body motions can be explicitly represented as follows

$$[m]_i[\phi_o]_i\{\ddot{\eta}_o\}_i = \{p\}_i \tag{16}$$

Premultiplying Equation 16 by $[\phi_o]_i^\intercal$ yields

$$\{\ddot{\eta}_o\}_i = [\phi_o]_i^\intercal\{p\}_i \tag{17}$$

where $[\phi_o]_i^\intercal[m]_i[\phi_o]_i = [I]$.
Suppose $\{p_o\}_i$ is the D'Alembert interia forces that are in equilibrium with the inertia loads, and therefore

$$\{p_o\}_i + [m]_i\{\ddot{u}_o\}_i = 0 \tag{18}$$

Equation 18 can be modified further using Equation 17, which yields

$$\begin{aligned} \{p_o\}_i &= -[m]_i\{\ddot{u}_o\}_i \\ &= -[m]_i[\phi_o]_i\{\ddot{\eta}_o\}_i \\ &= -[m]_i[\phi_o]_i[\phi_o]_i^\intercal\{p\}_i \end{aligned} \tag{19}$$

The equilibrated load system $\{p_e\}_i$ for the ith component can be represented as

$$\begin{aligned} \{p_e\}_i &= \{p\}_i + \{p_o\}_i \\ &= \{p\}_i - [m]_i[\phi_o]_i[\phi_o]_i^\intercal\{p\}_i \\ &= [\Psi]_i\{p\}_i \end{aligned} \tag{20}$$

where $[\Psi]_i = [I] - [m]_i[\phi_o]_i[\phi_o]_i^\intercal$ is the inertia-relief matrix.
The attachment modes ($[\phi_a]_i$) for the ith unrestrained component relative to the O constraints can be expressed as

$$\left[\begin{array}{cc:c} k_{ww} & k_{wl} & k_{wo} \\ k_{lw} & k_{ll} & k_{lo} \\ \hdashline k_{ow} & k_{ol} & k_{oo} \end{array}\right]_i \left[\begin{array}{c} \phi_w^a \\ \phi_l^a \\ \hdashline 0 \end{array}\right]_i = [\Psi]_i \left[\begin{array}{c} I \\ 0 \\ \hdashline 0 \end{array}\right]_i \tag{21}$$

Finally, the attachment modes are deduced from Equation 21 using the top-left partition of the stiffness matrix.
The constraint modes are assessed in the same manner as described in the preceding section. It is important to note that both attachment and constraint modes are instances of static response modes that manifest from constant external load and displacements, respectively.

Preprints (www.preprints.org) | NOT PEER-REVIEWED | Posted: 15 June 2022 doi:10.20944/preprints202206.0222.v1

For the ith substructure, Hintz's transformation matrix for dynamic analysis is represented by

$$[T_H]_i = \left[\begin{array}{c|c|c} I & 0 & \overline{\phi}_{Bn} \\ \hline \phi_c & \phi_a & \overline{\phi}_{In} \end{array}\right]_i \tag{22}$$

The reduced mass and stiffness matrix for the ith substructure can now be expressed as

$$\begin{aligned} [\bar{m}]_i &= [T_H]_i^\intercal [m]_i [T_H]_i \\ [\bar{k}]_i &= [T_H]_i^\intercal [k]_i [T_H]_i \end{aligned} \tag{23}$$

The constraints of interconnected substructures are implemented using a transformation matrix $[\beta]$. The final reduced structural mass and stiffness matrix can be represented as

$$\begin{aligned} [M_\mu] &= [\beta]^\intercal [\bar{M}_\mu][\beta] \\ [K_\mu] &= [\beta]^\intercal [\bar{M}_\mu][\beta] \end{aligned} \tag{24}$$

where

$$[\bar{M}_\mu] = \begin{bmatrix} \bar{m}_1 & & \\ & \ddots & \\ & & \bar{m}_\tau \end{bmatrix}, \quad [\bar{K}_\mu] = \begin{bmatrix} \bar{k}_1 & & \\ & \ddots & \\ & & \bar{k}_\tau \end{bmatrix}$$

Hintz's method for assessing free-free systems like launch vehicles, aircraft, and spacecraft is very efficient and is prevalently used by aerospace and space organizations.

2.3. State-Space Representation of Reduced-Order Model

The reduced structural matrices are stated in generalized coordinates in both the free-interface and fixed-interface component modal synthesis, as shown by Equations 11, and 24. Mode superposition and mode acceleration [69] both facilitate the transformation of modal displacements to physical displacements for a structure. In practice, during the solution phase of the modal synthesis procedures, the FEA-based software writes and stores the assembled reduced structural matrices and associated degrees of freedom in files. For instance, Ansys [66] stores this structural information in a binary file labeled "full." PyAnsys [70] is a free and open-source Python interface for Ansys that enables the retrieval and import of Ansys structural data into Python. It is desirable to express the reduced structural matrices obtained from FEA-based software in a platform-independent format. The present research considers state-space representation [71–73]. Expressing physical systems in a state-space representation is a well-established approach in control engineering; thus, most software platforms for modeling and simulating multi-domain dynamical systems include state-space blocks. The remainder of this section aims to establish a generalized state-space representation for the digital model of a reduced finite element model, and this approach applies to any arbitrary off-road vehicle.
For a reduced system, the undamped equation of motion can be expressed as

$$[M_r]\{\ddot{u}_r\} + [K_r]\{u_r\} = \{p_r\} \tag{25}$$

Although the reduced mass and stiffness matrices are symmetric, the non-zero off-diagonal elements render Equation 25 a system of coupled differential equations, which is computationally expensive to solve. In order to solve a system of coupled differential equations, the inertial and elastic decoupling of Equation 25 is essential, which is accomplished using the normal mode method. The equation of motion for the free vibration of the undamped reduced system is expressed as

$$[M_r]\{\ddot{u}_r\} + [K_r]\{u_r\} = \{0\} \tag{26}$$

 doi:10.20944/preprints202206.0222.v1

which is homogeneous. The solution of Equation 26 is of the form

$$\{u_r\} = [\phi]\{\eta_r\} \tag{27}$$

The modal matrix $[\phi]$ has the following orthogonality features in relation to the mass and stiffness matrices:

$$\begin{aligned} [\phi]^\intercal[M_r][\phi] &= [I] \\ [\phi]^\intercal[K_r][\phi] &= [\omega_*^2] \end{aligned} \tag{28}$$

where $[\omega_*^2] = diag(\omega_{*1}^2, \ldots, \omega_{*R}^2)$. The retained set of modes in the reduced-order model is a subset of the natural frequencies of the full-order finite element model. Mathematically, the relationship can be expressed as

$$\{\omega_*\} \subset \{\omega\} \tag{29}$$

where

$$\omega_{*i} \approx \omega_j \ : \ i \in \{1, \ldots, R\}, j \in \{1, \ldots, N\}$$

Thus, the coupled equations of motion in Equation 25 can be expressed as uncoupled equations of motion in modal coordinates using the orthogonality relations of the modal matrix, as

$$\{\ddot{\eta}_r\} + [\omega_*^2][\{\eta_r\} = [\phi]^\intercal\{p_r\} \tag{30}$$

Let us define $\eta_1, \dot{\eta}_1, \ldots, \eta_R, \dot{\eta}_R$ as the state variables, and for convenience, let us rename the state variables as $x_1, x_2, \ldots x_{2R}$, where

$$\begin{aligned} x_1 &= \eta_1 \\ x_2 &= \dot{\eta}_1 \\ &\vdots \\ x_{2R-1} &= \eta_R \\ x_{2R} &= \dot{\eta}_R \end{aligned} \tag{31}$$

Equation 31 can be expressed in the following manner

$$\begin{aligned} \dot{x}_1 &= x_2 \\ \dot{x}_2 &= \ddot{x}_2 \\ &\vdots \\ \dot{x}_{2R-1} &= x_{2R} \\ \dot{x}_{2R} &= \ddot{x}_{2R} \end{aligned} \tag{32}$$

Preprints (www.preprints.org) | NOT PEER-REVIEWED | Posted: 15 June 2022 doi:10.20944/preprints202206.0222.v1

Using Equations 30, 31, and 32, the equation of motion in principal coordinates can be expressed in terms of the state variables as

$$\begin{Bmatrix} \dot{x}_1 \\ \dot{x}_2 \\ \vdots \\ \dot{x}_{2R-1} \\ \dot{x}_{2R} \end{Bmatrix} = \begin{bmatrix} 0 & 1 & \dots & 0 & 0 \\ -\omega_{*1}^2 & 0 & \dots & 0 & 0 \\ \vdots & \vdots & \vdots & \vdots & \vdots \\ 0 & 0 & \dots & 0 & 1 \\ 0 & 0 & \dots & -\omega_{*R}^2 & 0 \end{bmatrix} \begin{Bmatrix} x_1 \\ x_2 \\ \vdots \\ x_{2R-1} \\ x_{2R} \end{Bmatrix} + [\phi]^{\mathsf{T}} \begin{Bmatrix} 0 \\ p_1 \\ \vdots \\ 0 \\ p_R \end{Bmatrix} \tag{33}$$

The modal displacements and velocities are obtained by solving Equation 33. For example, x_1, x_2 represent the modal displacement and velocity of the first retained degree of freedom. Let D be the number of degrees of freedom where the structure's displacement and velocity are to be monitored. Then, suppose $(S_i^D | i \in \{1, \dots, D\})$ and $(S_j | j \in \{1, \dots, R\})$ are the sequence of the set of degrees of freedom where the kinematics to be observed and the sequence of the set of retained degrees of freedom in the reduced structure, respectively. Let us now define a matrix $[\bar{C}]_{2D \times 2R}$ in the following way:

$$\begin{aligned} \bar{C}_{2i-1,2j+1} &= 1 : S_i^D = S_j, \forall i \in \{1, \dots, D\}, \forall j \in \{1, \dots, R\} \\ \bar{C}_{2i,2j+2} &= 1 : S_i^D = S_j, \forall i \in \{1, \dots, D\}, \forall j \in \{1, \dots, R\} \\ \bar{C}_{i,j} &= 0 : \text{otherwise} \end{aligned} \tag{34}$$

Let us define Λ and B as follows:

$$\Lambda^{ss} = \{\lambda^{ss} \in \mathbb{N}^+ | \lambda^{ss} \text{ is even and } \lambda^{ss} \leq 2R\}$$

and

$$B^{ss} = \{\beta^{ss} \in \mathbb{N}^+ | \beta^{ss} \text{ is even and } \beta^{ss} \leq 2R\}$$

The original modal matrix $[\phi]$ of the reduced structure can then be modified as follows:

$$\phi_{i,j}^{ss} = \begin{cases} \phi_{\frac{i}{2}, \frac{j}{2}} & : \forall i = \lambda^{ss} \in \Lambda^{ss}, \forall j = \beta^{ss} \in B^{ss} \\ 0 & : \text{otherwise} \end{cases} \tag{35}$$

where $[\phi^{ss}]$ is the reduced structure's modified modal matrix. The necessity for the aforementioned modification of the modal matrix is to accommodate the additional states related to the system velocity. The kinematic vector at selected degrees of freedom in physical coordinates can be derived using Equations 27, 34, and 35, yielding

$$\{y\} = [C]\{x\} \tag{36}$$

where $[C] = [\bar{C}][\phi^{ss}]$, and {x} is the system kinematics vector in modal coordinates. Furthermore, only a subset of the retained degrees of freedom in a reduced finite element model of a structure is subjected to external excitation. Suppose r_{in} be the number of excitations applied at distinct degrees of freedom of the structure, where $r_{in} \leq R$. Let us

Preprints (www.preprints.org) | NOT PEER-REVIEWED | Posted: 15 June 2022 doi:10.20944/preprints202206.0222.v1

further assume $(S_i^{r_{in}} | i \in \{1, \ldots, r_{in}\})$ is the sequence of the set of degrees of freedom where the external excitations are applied. As a result, Equation 33 can be rewritten as

$$\begin{Bmatrix} \dot{x}_1 \\ \dot{x}_2 \\ \vdots \\ \dot{x}_{2R-1} \\ \dot{x}_{2R} \end{Bmatrix} = \begin{bmatrix} 0 & 1 & \ldots & 0 & 0 \\ -\omega_{*1}^2 & 0 & \ldots & 0 & 0 \\ \vdots & \vdots & \vdots & \vdots & \vdots \\ 0 & 0 & \ldots & 0 & 1 \\ 0 & 0 & \ldots & -\omega_{*R}^2 & 0 \end{bmatrix} \begin{Bmatrix} x_1 \\ x_2 \\ \vdots \\ x_{2R-1} \\ x_{2R} \end{Bmatrix} + [\phi^{ss}]_{2R \times 2R} [\beta^p]_{2R \times r_{in}} \begin{Bmatrix} |p_1| \\ \vdots \\ |p_{r_{in}}| \end{Bmatrix}_{r_{in} \times 1} \tag{37}$$

where $|p_j| \; \forall j \in \{1, \ldots, r_{in}\}$ is the magnitude of jth externally applied excitation in physical coordinates, and $[\beta^p]$ is a Boolean matrix defined as follows

$$\begin{aligned} \beta_{2i,j}^p &= 1 \quad : S_j^{r_{in}} = S_i, \forall i \in \{1, \ldots, R\}, \forall j \in \{1, \ldots, r_{in}\} \\ \beta_{i,j}^p &= 0 \quad : \text{otherwise} \end{aligned} \tag{38}$$

Finally, the state-space representation of a reduced finite element model can be expressed using Equation 37 as

$$\begin{aligned} \{\dot{x}\} &= [A]\{x\} + [B]\{z\} \\ \{y\} &= [C]\{x\} + [D]\{z\} \end{aligned} \tag{39}$$

where the matrices are represented as

$$\begin{aligned} [A] &= \begin{bmatrix} 0 & 1 & \ldots & 0 & 0 \\ -\omega_{*1}^2 & 0 & \ldots & 0 & 0 \\ \vdots & \vdots & \vdots & \vdots & \vdots \\ 0 & 0 & \ldots & 0 & 1 \\ 0 & 0 & \ldots & -\omega_{*R}^2 & 0 \end{bmatrix} \\ [B] &= [\phi^{ss}][\beta^p] \\ [C] &= [\bar{C}][\phi^{ss}] \end{aligned} \tag{40}$$

and

$$[D] = [0]$$

The physical displacements and velocities at the coordinates where the encoders are attached to a structure are represented by the output vector $\{y\}$.

3. Evaluation Criteria

It is essential to validate the accuracy of the dynamic reduction approaches outlined in the preceding section in the context of off-road vehicles. In general, the quality of the reduced finite element models obtained by these dynamic reduction approaches characterizes their accuracy. The frequencies and mode shapes of a reduced model are typically compared to those of the full-order finite element model or reference model to determine its accuracy. An important metric for evaluating the precision of dynamic reduction techniques is the deviation of the natural frequencies from the full-order model for the reduced

Preprints (www.preprints.org) | NOT PEER-REVIEWED | Posted: 15 June 2022 doi:10.20944/preprints202206.0222.v1

structure. To represent the frequency deviations between the reduced-order model and the full-order model in mathematical terms, we can use

$$\epsilon_i = \left| \frac{\omega_{*i} - \omega_i}{\omega_i} \right| \times 100\% \tag{41}$$

where ϵ_i represents the percentage error between the ith reduced-order and full-order mode, $i \in \{Q\}$, and where $\{Q\} = \{1, \ldots, R\} \cap \{1, \ldots, N\}$. For the most part, the client defines the maximum frequency deviations permitted.

The cross-orthogonality check, also known as the modal vector orthogonality check, is often used to assess the quality of reduced-order finite element models in conjunction with the frequency deviation check. In the cross-orthogonality check [74], the mass normalized modal matrix ($[\phi]$) obtained by the modal analysis is primarily employed in combination with the mass matrix ($[M_r]$) of the reduced-order model to assess the orthogonality of the modal vectors. Because reduced-order models have linearly independent degrees of freedom, each modal vector in the modal matrix should be orthogonal to the other vectors. As a result, the orthogonality relations may be expressed as

$$\{\phi_i\}^\intercal [M_r] \{\phi_j\} = \begin{cases} 0 : i \neq j \\ 1 : \text{otherwise} \end{cases} \tag{42}$$

Dynamic reduction techniques are based on the notion of transforming a substructure's physical coordinates into a set of generalized coordinates and then truncating modal coordinates to obtain a reduced set of equations for the system. As a consequence, exact system solutions with reduced computational load are obtained over a limited frequency range. Modal truncation was essential in the past for structural finite element model analysis when the number of degrees of freedom exceeded the computing capability. In the last two decades, the exponential increase in processor performance, the introduction of general-purpose graphics processing units, and the availability of efficient and accurate numerical algorithms have essentially mitigated the computational constraints in the design and analysis processes of earlier times. Nonetheless, in the context of Industry 4.0, dynamic reduction methods are significant for the development of physics-based digital models for off-road vehicles. In essence, virtual models consist of the modal characteristics of physical off-road vehicles. In addition, digital twins are intended to emulate the simultaneous activities of their physical counterparts operating in an industrial environment. Consequently, solving the equation of motion in real-time that encompasses the complete set of modes constituting the virtual system is impractical. As a result, dynamic reduction-based reduced-order models are appropriate for accomplishing the requirements.

In practice, for well-formulated structural analysis problems, the lower order modes derived by dynamic reduction methods are extremely accurate, but substantial inaccuracies may occur in the higher frequency range. Furthermore, the general principle for dynamic reduction is to incorporate subcomponent modes up to 1.5–2.0 times the frequency range of interest [75], which is a value that the client specifies. However, certain subcomponents for off-road vehicles may have all the modal components exceeding the frequency range of interest. In such circumstances, the number of coordinates to be retained for each subcomponent is specified without explicitly defining the frequency range in the analysis. Subsequently, during the final system synthesis, the coordinate system obtained by synthesizing individual substructures is truncated to the desired frequency range for the overall structure.

Vibration analysis of off-road vehicles tends to focus on the lower frequency bands and the equations of motion comprised of these modes, which eventually represent their virtual models. As the number of modes incorporated into the digital model increases, so does the computational cost, which eventually deters the simulation from being synchronized with the real-time activity of its physical counterpart. Furthermore, the simulation result

 doi:10.20944/preprints202206.0222.v1

of digital models comprised of fewer modal components may deviate from the actual behavior of the physical structure. In this research, virtual models with frequencies ranging from 0 to 30 Hz in 5 Hz steps are used to analyze the trade-off between simulation accuracy and duration.

Most textual and graphical programming platforms have built-in state-of-the-art libraries of solvers to determine the states of the explicit continuous-time state-space models given by Equation 39. It is common for these models to be simulated using variable-step solvers or fixed-step solvers, respectively. Instead of solving a model at regular intervals, the former solvers alter the step size during simulation, whereas the latter does it consistently. The adoption of fixed-step solvers for the simulation of digital models is appropriate since data is acquired from sensors connected to the physical device at fixed intervals.

During simulation, all fixed-step solvers but ode14x compute the succeeding state as

$$x(t+1) = x(t) + h\dot{x}(t) \tag{43}$$

ode14x uses a combination of Newton's method and extrapolation from the current state to compute the succeeding state of the model, which yields

$$x(t+1) = x(t) + h\dot{x}(t+1) \tag{44}$$

The method used to evaluate $\dot{x}$ in Equations 43 and 44 is algorithm-specific and also reliant on the algorithm's order. In this research, to evaluate their efficacy, the digital models obtained by the dynamic reduction methods are solved using the following fixed-step solvers:

1. ode4 (fourth-order Runge-Kutta formula)[76]
2. ode5 (fifth-order Dormand-Prince formula) [77]
3. ode8 (eighth-order Dormand-Prince formula) [78], and,
4. ode14x [76]

The complexity of the algorithms rises as the order n in ode$n$ increases. However, as the computational complexity grows, so does the accuracy of the result. In addition, a smaller step size enhances accuracy, but at the same time, it increases the time complexity. It is important to note that large time steps render the numerical solutions of certain models numerically unstable. With all of these factors in mind, it is essential to identify the optimal solver that achieves the trade-off between acceptable accuracy and the duration of simulation of the virtual model so that it does not exceed the operational time of its physical counterpart. To summarize, the quality of the reduced-order models obtained from model order reduction methods will be assessed using frequency deviation checks and cross-orthogonality checks. Additionally, the solutions of the digital models for several frequency ranges utilizing the stated solvers will be assessed in terms of accuracy and simulation runtime.

4. Results

This section presents a comprehensive assessment of the efficacy of dynamic model reduction approaches based on the evaluation methodology outlined in Section 3. The structure utilized to compare the dynamic reduction approaches is an existing commercial off-road vehicle. The structure was designed, modeled, and analyzed using the Ansys 2020R2 platform. Due to confidentiality considerations, the structure shown in Figure 1 is only a partial line diagram. The overall mass of the structure is 359 Tonnes, and translational movement is restricted along the X and Z-axes, while travel along the Y-axis is unrestricted. The built-in libraries of the dynamic reduction methods outlined in Section 2 are available in Ansys 2020R2, and [79,80] provides a detailed description of the procedure to develop reduced-order models from full-order finite element models using these libraries.

Preprints (www.preprints.org) | NOT PEER-REVIEWED | Posted: 15 June 2022 doi:10.20944/preprints202206.0222.v1

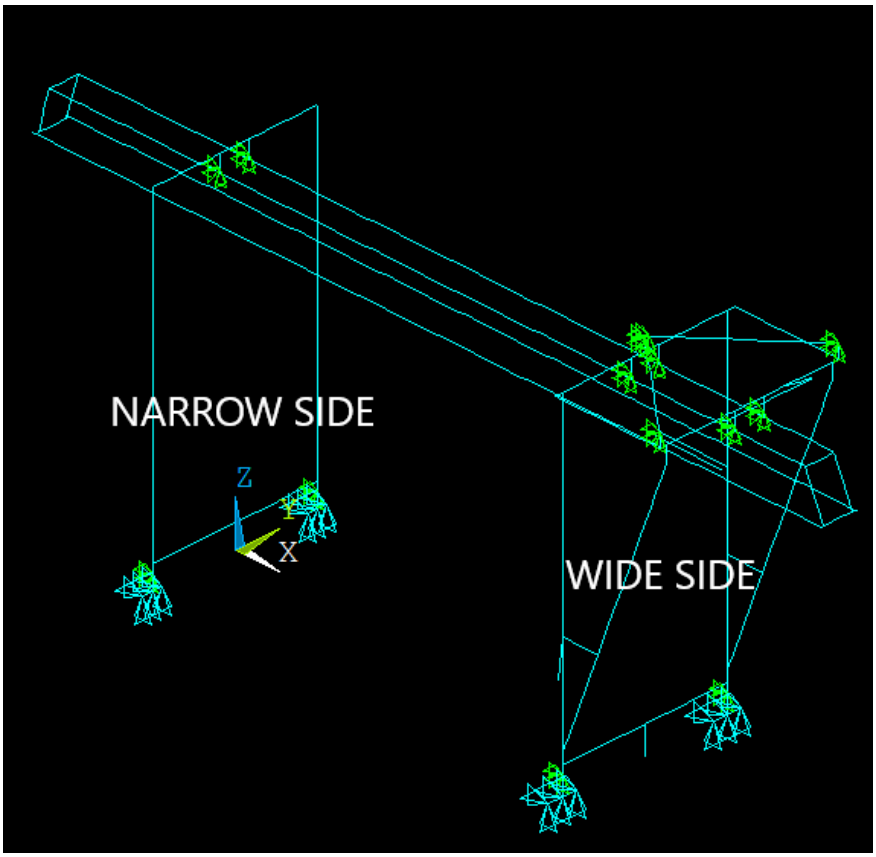

Figure 1. Line Diagram with Boundary Conditions and Couplings for the structure.

Table 1 shows a comparison of the modes up to 30 Hz between full-order and reduced-order models obtained by dynamic reduction techniques.

Table 1. Full-Order and Reduced-Order Modes.

Mode No.	FULL-ORDER	FREE-INTERFACE CMS	FIXED-INTERFACE CMS
	Freq (Hz)	Freq (Hz)	Freq (Hz)
1	0.0000	0.0000	0.0000
2	0.1857	0.1857	0.1857
3	0.4302	0.4302	0.4302
4	1.0493	1.0492	1.0492
5	1.1142	1.1142	1.1142
6	1.8422	1.8414	1.8414
7	2.0013	2.0011	2.0011
8	2.2746	2.2712	2.2712
9	2.4619	2.4612	2.4612
10	2.9458	2.9453	2.9453
11	3.8005	3.7995	3.7995
12	4.0081	4.0072	4.0072
13	4.2623	4.2613	4.2613
14	4.4271	4.4151	4.4150
15	4.8720	4.8518	4.8517
16	5.0604	5.0485	5.0485
17	5.1830	5.1753	5.1753
18	5.6314	5.5985	5.5986
19	5.7793	5.7758	5.7758

 doi:10.20944/preprints202206.0222.v1

20	5.9551	5.9517	5.9518
21	6.1300	6.1293	6.1292
22	6.2820	6.2816	6.2816
23	6.5562	6.5531	6.5531
24	6.9902	6.9806	6.9806
25	7.2392	7.2325	7.2325
26	7.4208	7.4186	7.4186
27	7.5028	7.5020	7.5020
28	7.6217	7.6175	7.6175
29	7.7598	7.7588	7.7588
30	7.9304	7.9310	7.9310
31	7.9935	7.9813	7.9813
32	8.0515	8.0427	8.0427
33	8.3542	8.3501	8.3502
34	8.4016	8.3975	8.3977
35	8.5372	8.5362	8.5363
36	8.5915	8.5831	8.5831
37	8.6763	8.6649	8.6649
38	8.8309	8.8182	8.8182
39	9.0159	9.0136	9.0137
40	9.0726	9.0656	9.0655
41	9.1020	9.1078	9.1078
42	9.3330	9.3323	9.3324
43	9.7096	9.7072	9.7074
44	9.7463	9.7372	9.7374
45	10.0290	10.0262	10.0263
46	10.1870	10.1680	10.1681
47	10.4320	10.4292	10.4296
48	11.0240	11.0229	11.0231
49	11.9730	11.9713	11.9714
50	11.9930	11.9919	11.9920
51	12.0290	12.0277	12.0277
52	12.1350	12.1325	12.1326
53	12.4540	12.4287	12.4288
54	13.2190	13.2155	13.2162
55	13.5810	13.5752	13.5756
56	13.8690	13.8652	13.8666
57	14.2990	14.2898	14.2900
58	14.7240	14.6956	14.6957
59	14.8700	14.8130	14.8132
60	15.2040	15.1943	15.1942
61	15.3810	15.3788	15.3792
62	16.6140	16.6105	16.6110
63	16.6540	16.6420	16.6415
64	16.7850	16.7810	16.7815
65	17.0350	17.0039	17.0039
66	17.1120	17.1068	17.1078
67	17.2230	17.2216	17.2212
68	17.8190	17.8141	17.8161
69	18.3840	18.3698	18.3721
70	18.7200	18.7067	18.7073
71	18.8380	18.8216	18.8219

 doi:10.20944/preprints202206.0222.v1

72	18.9780	18.9641	18.9645
73	19.4900	19.4869	19.4882
74	19.5310	19.5261	19.5267
75	19.7960	19.7869	19.7893
76	19.9100	19.8781	19.8793
77	20.3080	20.3112	20.3124
78	20.7510	20.7381	20.7436
79	21.1300	21.1500	21.1504
80	21.3580	21.3469	21.3482
81	21.5700	21.5492	21.5493
82	21.7170	21.6348	21.6353
83	21.8040	21.8018	21.8019
84	22.0530	22.0131	22.0144
85	22.3150	22.3055	22.3086
86	22.4830	22.4724	22.4725
87	22.7500	22.6872	22.6877
88	23.2110	23.1199	23.1202
89	23.3010	23.2927	23.2955
90	23.3880	23.3803	23.3822
91	24.0510	23.9223	23.9285
92	24.2010	24.1674	24.1707
93	24.2800	24.2165	24.2187
94	24.3390	24.3309	24.3325
95	24.7000	24.5120	24.5120
96	25.0620	25.0344	25.0341
97	25.1270	25.0614	25.0636
98	25.3970	25.3898	25.3908
99	25.4890	25.5556	25.5579
100	25.7190	25.7176	25.7208
101	25.7810	25.7567	25.7612
102	26.2300	26.1940	26.1973
103	26.4390	26.4237	26.4268
104	26.4940	26.4457	26.4505
105	26.8210	26.8180	26.8201
106	26.9660	26.9501	26.9515
107	27.0410	27.0264	27.0275
108	27.1310	27.1217	27.1219
109	27.2620	27.2582	27.2630
110	27.4920	27.5396	27.5461
111	27.8520	27.8642	27.8690
112	28.2750	28.2502	28.2612
113	28.4250	28.4160	28.4172
114	28.7100	28.7304	28.7353
115	28.9110	28.9312	28.9342
116	29.0080	29.0032	29.0053
117	29.3980	29.4209	29.4278
118	29.6380	29.6299	29.6304
119	29.6620	29.6699	29.6710
120	29.9190	29.8785	29.8789

Preprints (www.preprints.org) | NOT PEER-REVIEWED | Posted: 15 June 2022 doi:10.20944/preprints202206.0222.v1

Figure 2 depicts that the frequency deviation of the reduced-order model from the full-order finite element model for both free-interface and fixed-interface modal synthesis is less than 0.8% over a frequency range of 0–30 Hz.

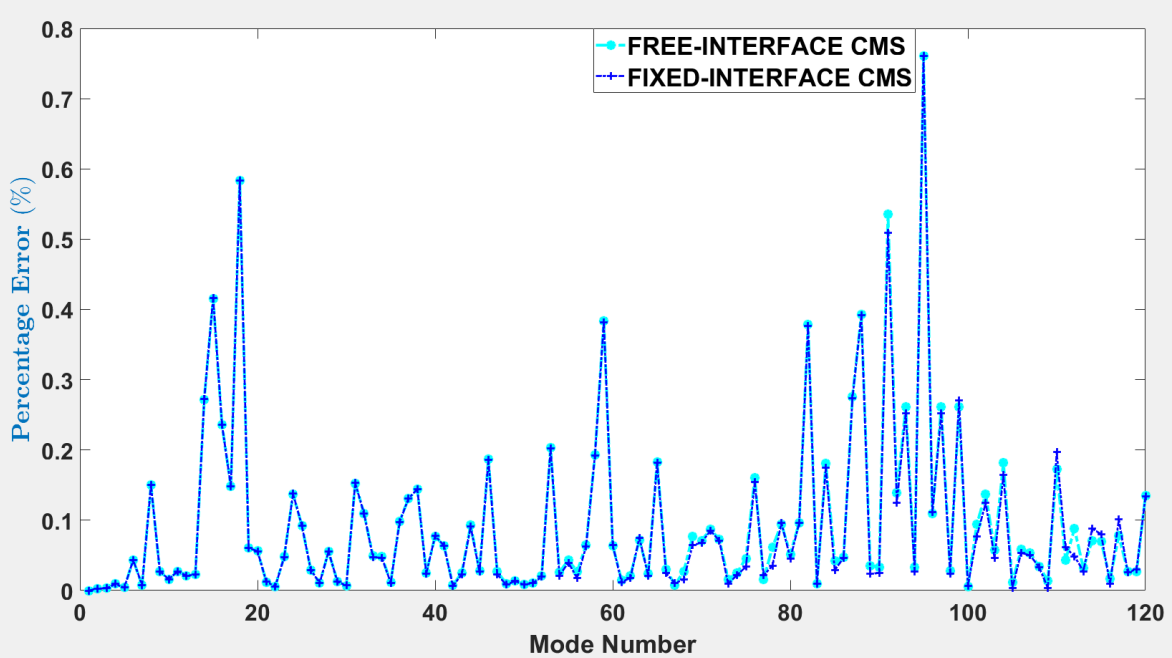

Figure 2. Percentage deviations of modes.

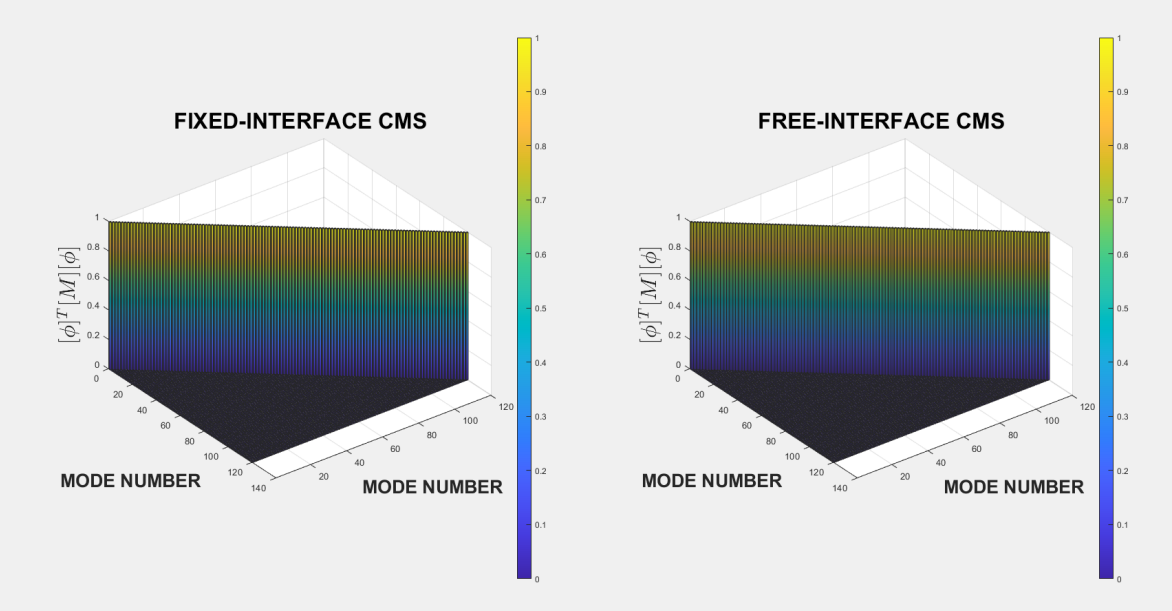

Figure 3. Modal Vector Orthogonality Checks of the Reduced-Order Models.

Preprints (www.preprints.org) | NOT PEER-REVIEWED | Posted: 15 June 2022 doi:10.20944/preprints202206.0222.v1

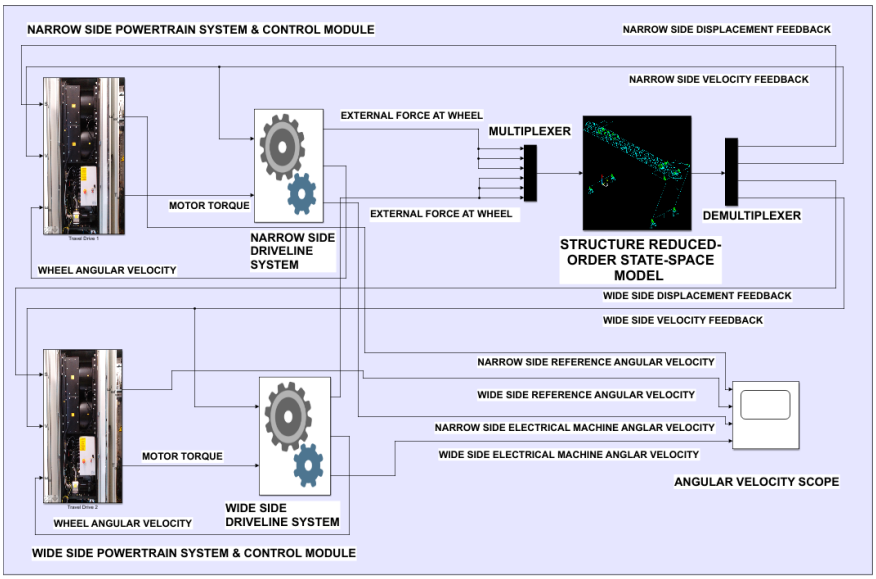

Figure 4. Simulation Model for the Structure in MATLAB.

Figure 3 shows the modal vector orthogonality verification of the component modal synthesis-based reduced-order model for modes up to 30 Hz. The diagonal terms are unity, but all off-diagonal terms are near to zero for the reduced-order models obtained from both fixed-interface and free-interface component modal synthesis, as shown in the figure, which is consistent with the orthogonality relations specified in Equation 42.
Figure 4 illustrates the digital model of the structure created utilizing either of the modal synthesis methods and integrating the corresponding driveline, electrical, and powertrain control modules in the MATLAB Simulink environment.
The structure has twelve rigid wheels with a 710 mm diameter, three of which are attached to each of its four corners. Additionally, the structure is driven by six electrical machines, three on each side, which means that three wheels on each side are driven by electrical machines while the other three are undriven. The rated power of each electrical machine is 165 kW, the rated speed is 1413 rpm, and the rated frequency is 60 Hz. An encoder is attached to one of the driving wheels on either side. The driveline system also includes gears with a gear ratio of 26.28. The powertrain control module is composed of a proportional-integral controller (PI controller) with gain parameters (k_P and k_I) that are a linear, monotonically decreasing function of the wheel's instantaneous angular velocity in the acceleration regime and a constant in the steady-state regime, and a linear, monotonically increasing function of the wheel's instantaneous angular velocity in the deceleration regime. As coded in the control module, the piecewise reference trapezoidal trajectory is as follows:

$$\Omega(t_i, \Omega_r, v, s) = \begin{cases} \Theta_a t_i^{as} & : t_i = t_i^{as}, s_i < s_d, v_i < v_m, \\ & \Omega(t_i^{as}) < \Omega_r \\ \Omega_r & : t_i = t_i^{as}, s_i < s_d, v_i < v_m, \\ & \Omega(t_i^{as}) = \Omega_r \\ \Omega_{t_{i-1}^{as}} & : t_i = t_i^{as}, s_i < s_d, v_i = v_m \\ \Theta_d t_i^d & : t_i = t_i^d, s_i \geq s_d \end{cases} \tag{45}$$

The simulation scenario is described as follows: the structure is allowed to travel a distance of 30 m along the Y-axis; subsequently, the braking regime is initiated, where the electrical machines reverse the direction of rotation; and ultimately, the simulation terminates as soon as the wheels come to a standstill. The structure is permitted to attain a maximum velocity of 2 m/s at any instant in time. The control modules, as illustrated in Figure 4, monitor both displacement and velocity at the output ports of the reduced-order model's

Preprints (www.preprints.org) | NOT PEER-REVIEWED | Posted: 15 June 2022 doi:10.20944/preprints202206.0222.v1

state-space model representation through a feedback loop. In practice, the control module monitors the encoder signals for displacement and velocity.
Initially, a fixed-interface cms-based reduced-order model with modes up to 30 Hz is used to explain the dynamics of the structure, followed by a comparison of the simulation results of the reduced-order models obtained from both dynamic reduction methods. Figure 5 illustrates the simulation outcomes for the wheel's angular velocity and displacement for both the structure's narrow and wide sides. As evident from Figure 5, the braking regime commences as soon as the structure traverses 30 m, and eventually the wheels come to a complete halt at 25.5 s. In Figure 6, the simulation results for the motor angular velocities

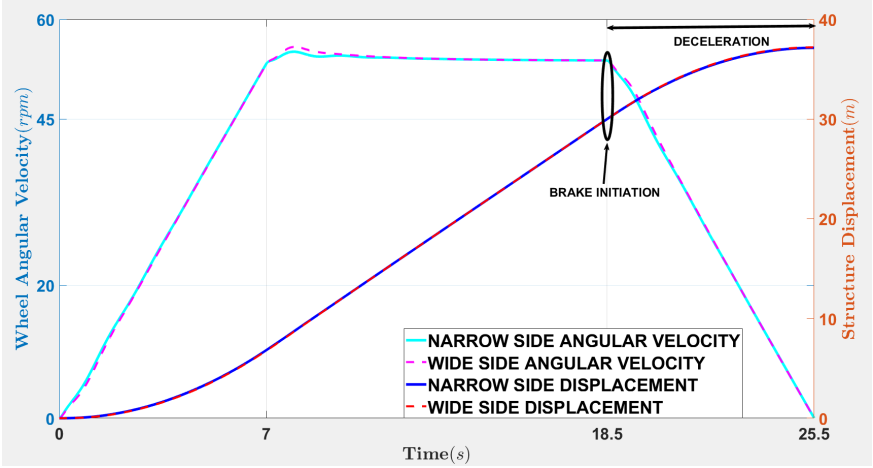

Figure 5. Wheel Angular Velocity and Displacement for the structure.

and translational velocities at the narrow and wide sides are depicted. Additionally, Figure 6 depicts the acceleration phase, which lasts until the structure reaches its maximum velocity of 2 m/s, at which point it maintains a constant velocity until the braking process begins. Figure 7 depicts the torque at the gear output side for both narrow and wide

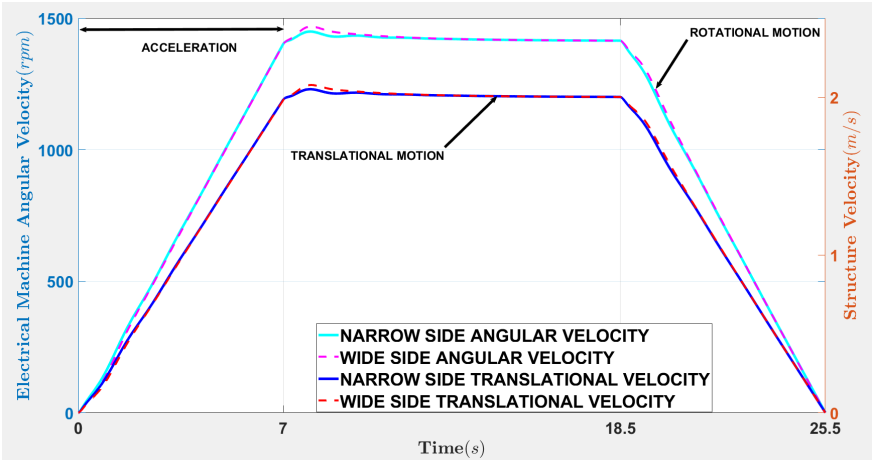

Figure 6. Electrical Machine Angular Velocity and Linear Velocity of the structure.

sides, the angular velocities of the electrical machines on the narrow and wide sides, and the reference trajectory of the angular velocity that the structure is expected to track. In addition, Figure 7 shows the torque necessary to keep the angular velocities consistent with the reference ramp.
The minimum and maximum coordinates spanned by the structure along the X, Y, and Z-axes are $(-19.4, 63.5)$, $(-10.14, 10.14)$, and $(0, 35.88)$ respectively, whereas the center of mass (X, Y, Z) is at $(28.317, -0.417, 21.269)$, where the units are in the SI system. The minimum and maximum span of the coordinates along the X-axis are on the narrow and wide

Preprints (www.preprints.org) | NOT PEER-REVIEWED | Posted: 15 June 2022 doi:10.20944/preprints202206.0222.v1

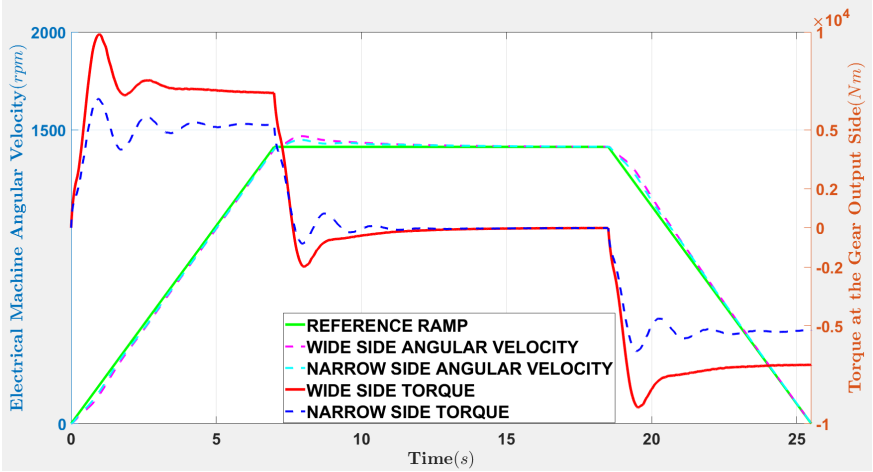

Figure 7. Electrical Machine Angular Velocity and Torque at the gear output side.

sides, respectively. As a result, the structure's mass is asymmetrically distributed towards the wide sides along the X-axis, the horizontal axis orthogonal to the direction of travel. As a direct consequence of the skewed mass distribution along the X-axis, there is a greater demand for torque from the wide side motors than from the narrow side motors. The simulation result shown in Figure 7 corroborates the justification. Furthermore, owing to asymmetrical mass distribution, the instantaneous velocities of the narrow and wide sides often differ during travel, as shown by the simulation result in Figure 5. Figure 8 illustrates the geometric deformation of the structure as a consequence of the mass imbalance and application specifics. In other words, if $s_N(t)$ and $s_W(t)$ are the displacements at the narrow and wide sides, respectively, at any simulation epoch t, then the difference in displacement at that instance is given by $(s_N(t) - s_W(t))$, and $(s_N(t) - s_W(t)) \neq 0$ indicates geometric distortion in the structure.

Fixed-interface component modal synthesis-based reduced-order models constituting

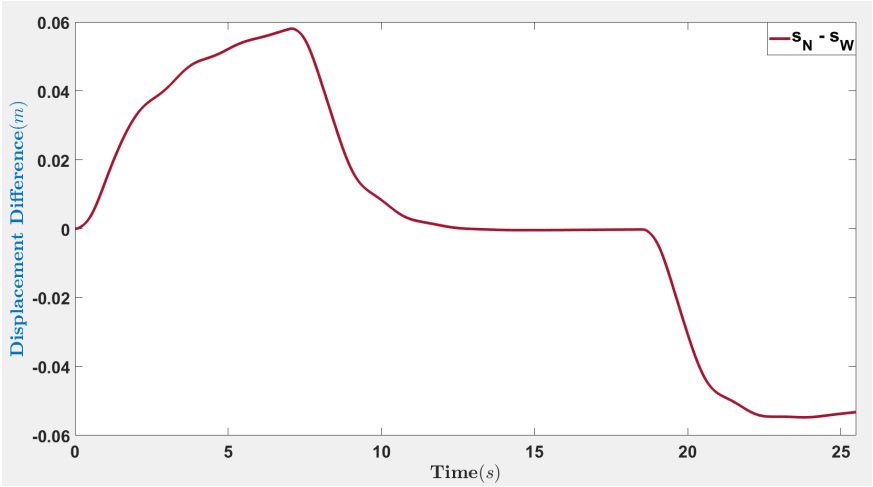

Figure 8. Dissimilar Displacements at Narrow and Wide Sides.

modes up to 30 Hz have been used in the simulations thus far. Figure 9 exhibits the simulation results of the angular velocity for the electrical machine at the wide side for reduced-order models with modes up to 5 Hz, 10 Hz, and 30 Hz. The simulation result for the ROM with modes up to 5 Hz differs from the results of the other two ROMs, while there is no substantial variance between the simulation results of the ROMs with frequency ranges of 10 Hz and 30 Hz. Reduced-order models based on free-interface component modal synthesis yielded the same simulation results. Both fixed-interface component modal synthesis and free-interface component modal synthesis-based ROMs with modes ranging

Preprints (www.preprints.org) | NOT PEER-REVIEWED | Posted: 15 June 2022 doi:10.20944/preprints202206.0222.v1

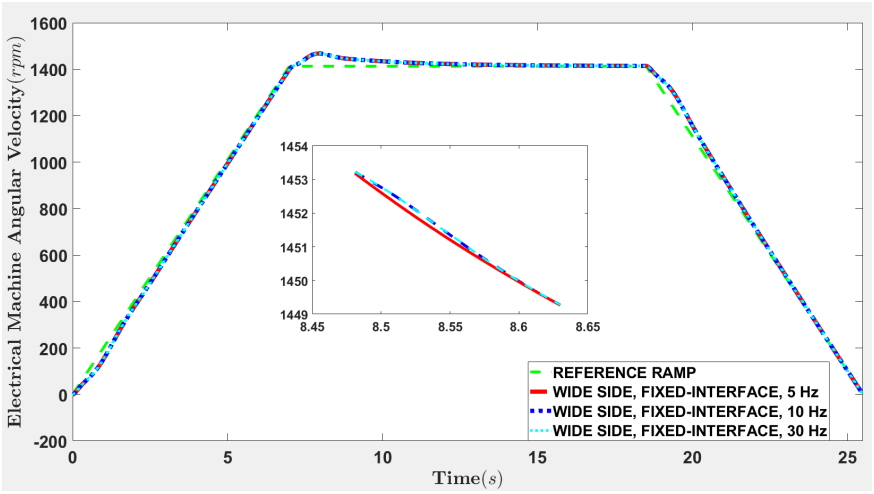

Figure 9. Wide Side Electrical Machine Angular Velocity for Fixed-Interface ROMs with varying Modes.

from 10 Hz to 30 Hz had almost indistinguishable simulation outcomes. Furthermore, there is no significant difference in simulation outcomes between ROMs based on fixed-interface and free-interface component modal synthesis methods. It is conceivable that the similarities in simulation outcomes are attributable to the fact that the reduced-order models developed using both approaches have almost identical modes.

To this point, comprehensive findings of the outcomes for various simulation scenarios for reduced-order models based on dynamic reduction techniques have been provided. The remainder of this section concentrates on the elapsed time for the solvers to execute the simulation models, which is one of the performance metrics to identify the appropriate dynamic reduction method. A computer with an Intel Core $i7-8700$ CPU and 16 GB of RAM was utilized to perform all numerical simulations.

Given that the primary objective of the reduced-order model-based virtual model is to emulate the physical counterpart, a solver with a runtime longer than the physical counterpart's real-time activity is inappropriate. Figure 10 shows the time it takes to execute various numerical solvers to simulate digital models with varying frequency ranges. To be precise, the elapsed periods shown in Figure 10 are the averages of the elapsed times for 25 recurring instances. The time step used for all the fixed-step solvers is $1e-04$. The elapsed time to numerically solve the digital models is a monotonically increasing function of the frequency ranges, as seen in Figure 10. As depicted in Figure 10 , ode8, ode5, and ode14x have runtimes that exceed 25.5 s, the upper bound for admissible simulation time, and so are inadequate to satisfy the metrics. Ode4 outperforms ode8, ode5, and ode14x in terms of execution time. However, ode3, which employs the Bogacki-Shampine formula, is the most economical approach for numerically solving digital models of off-road vehicles in terms of elapsed time. Figure 10 further illustrates that in most frequency ranges, digital models represented by free-interface component modal synthesis require less time to execute than digital models based on fixed-interface component modal synthesis for most solvers. Although there is no substantial difference in accuracy between fixed and free-interface component modal synthesis-based digital models, free-interface component modal synthesis-based digital models for off-road vehicles are deemed appropriate in a computing resource-constrained setting.

5. Conclusion

The development of digital twins for off-road vehicles is at an emerging stage. There are several impediments to developing and executing virtual models for off-road vehicles. Firstly, the manual generation of off-road vehicle virtual models is inconvenient due to the sheer number and diversity of existing and operational off-road vehicles. Furthermore, de-

Preprints (www.preprints.org) | NOT PEER-REVIEWED | Posted: 15 June 2022 doi:10.20944/preprints202206.0222.v1

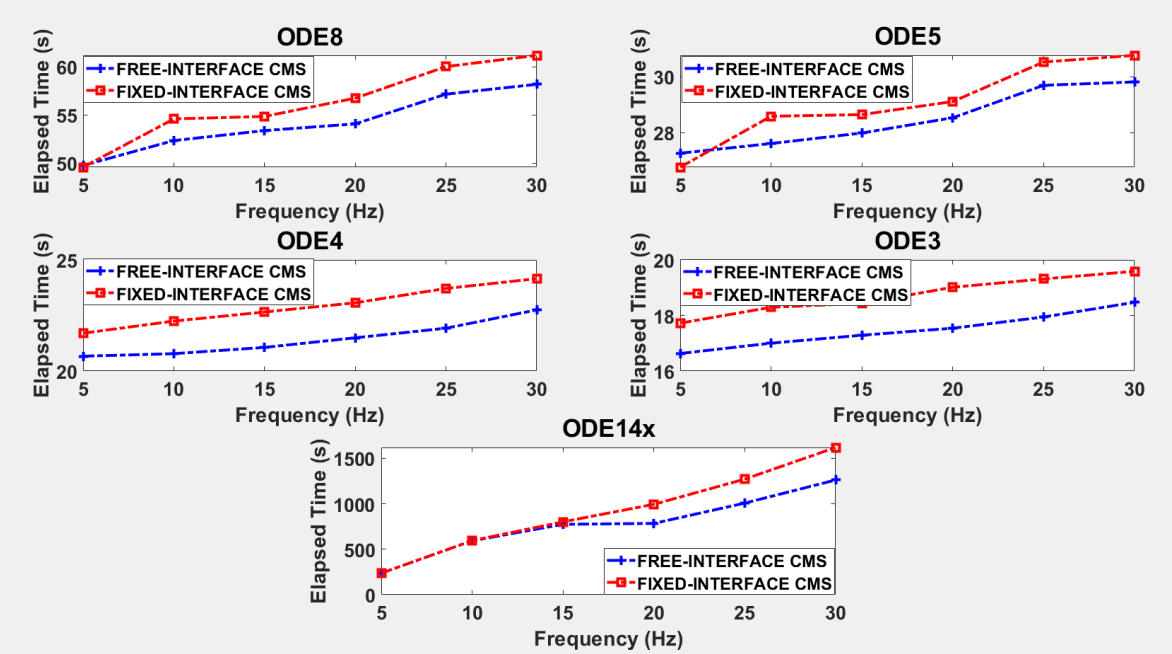

Figure 10. Elapsed time for various frequency ranges of digital models.

signing custom electrical, powertrain, and control components on an FEA-based platform is complicated. Improvements to the modeling and simulation capabilities of FEA-based software are certainly plausible, but such procedures for upgrade are challenging. Although the uncluttered syntax renders modeling the control and powertrain systems straightforward, structural design and analysis are complicated in problem-solving environments. This article proposes a method for developing digital models by using reduced-order models of existing structures on the same design platform rather than re-modeling them on a different platform, resulting in no significant additional effort. The development of reduced-order models from full-order structural finite-element models and subsequently representing the reduced-order models in state-space representation can be automated, enabling the development of structural virtual models with minimal additional effort and time.
The main contributions of the article are:

- A comprehensive review of the dynamic reduction methods, the libraries of which are available as built-in packages on most FEA-based platforms. The dynamic reduction methods eventually facilitate the development of the reduced-order models of the existing and operating structures.
- A mathematical derivation of the state-space representation of the reduced-order models.
- Establishing the performance metrics for evaluating dynamic reduction methods.
- Identifying the most appropriate dynamic reduction approach for developing digital twins for off-road vehicles.
- A comparison of the numerical solvers in the problem-solving platforms.
- Selection of the optimal numerical solver to simulate the digital models for off-road vehicles.
- Identifying the lower bound of the frequency range is necessary and sufficient for developing reduced-order models for off-road vehicles.

The following are the rationale for state-space representation of the reduced-order models:

- Most commercial textual and graphical programming platforms have built-in blocks to represent the state-space models.
- It facilitates the modeling of virtual models based on ROMs incorporating structural damping.

- While performing industrial operations, the configuration of specific components within a structure varies, modifying the full-order finite element model, which subsequently alters the modal characteristics of the overall structure. As a consequence, the reduced-order model changes as well. In these scenarios, the time-varying state-space model can be used on textual and graphical programming platforms to simulate digital models based on changing ROMs.

The simulation results demonstrate that the outputs of digital models based on free-interface and fixed-interface component modal synthesis are not substantially different. However, owing to the reduced computational overload, virtual models based on free-interface component modal synthesis are more appropriate in resource-constrained settings.

Author Contributions: Conceptualization, S.M.; Methodology, S.M.; Software, S.M.; Validation, S.M.; Formal analysis, S.M.; Investigation, S.M.; Resources, S.M.; Data curation, S.M.; Writing—original draft preparation, S.M.; Writing—review and editing, S.M., D.R., and J.W.; Visualization, S.M.; Supervision, D.R. and J.W.; Project Administration, S.M., D.R., and J.W.; Funding Acquisition, D.R. and J.W. All authors have read and agreed to the published version of the manuscript.

Funding: The authors would like to thank Munster Technological University for providing the opportunity to undertake this research. This work was supported, in part, by Science Foundation Ireland grant 13/*RC*/2094_*P*2 and co-funded under the European Regional Development Fund through the Southern & Eastern Regional Operational Programme to Lero - the Science Foundation Ireland Research Centre for Software (www.lero.ie).

Institutional Review Board Statement: Not applicable.

Informed Consent Statement: Not applicable.

Acknowledgments: This paper and research behind it would not have been possible without the support of the IMaR team in the Munster Technological University.

Conflicts of Interest: The authors declare no conflict of interest.

References

1. Lasi, H.; Fettke, P.; Kemper, H.G.; Feld, T.; Hoffmann, M. Industry 4.0. *Business & information systems engineering* **2014**, *6*, 239–242.
2. Gilchrist, A. *Industry 4.0: the industrial internet of things*; Springer, 2016.
3. Raj, A.; Dwivedi, G.; Sharma, A.; de Sousa Jabbour, A.B.L.; Rajak, S. Barriers to the adoption of industry 4.0 technologies in the manufacturing sector: An inter-country comparative perspective. *International Journal of Production Economics* **2020**, *224*, 107546.
4. Ghobakhloo, M. Industry 4.0, digitization, and opportunities for sustainability. *Journal of cleaner production* **2020**, *252*, 119869.
5. Bai, C.; Dallasega, P.; Orzes, G.; Sarkis, J. Industry 4.0 technologies assessment: A sustainability perspective. *International journal of production economics* **2020**, *229*, 107776.
6. Kumar, R.; Singh, R.K.; Dwivedi, Y.K. Application of industry 4.0 technologies in SMEs for ethical and sustainable operations: Analysis of challenges. *Journal of cleaner production* **2020**, *275*, 124063.
7. Silvestri, L.; Forcina, A.; Introna, V.; Santolamazza, A.; Cesarotti, V. Maintenance transformation through Industry 4.0 technologies: A systematic literature review. *Computers in Industry* **2020**, *123*, 103335.
8. Yadav, G.; Kumar, A.; Luthra, S.; Garza-Reyes, J.A.; Kumar, V.; Batista, L. A framework to achieve sustainability in manufacturing organisations of developing economies using industry 4.0 technologies' enablers. *Computers in industry* **2020**, *122*, 103280.
9. Benitez, G.B.; Ayala, N.F.; Frank, A.G. Industry 4.0 innovation ecosystems: An evolutionary perspective on value cocreation. *International Journal of Production Economics* **2020**, *228*, 107735.
10. Culot, G.; Nassimbeni, G.; Orzes, G.; Sartor, M. Behind the definition of Industry 4.0: Analysis and open questions. *International Journal of Production Economics* **2020**, *226*, 107617.
11. Santos, R.C.; Martinho, J.L. An Industry 4.0 maturity model proposal. *Journal of Manufacturing Technology Management* **2020**.
12. Oztemel, E.; Gursev, S. Literature review of Industry 4.0 and related technologies. *Journal of Intelligent Manufacturing* **2020**, *31*, 127–182.
13. Pejic-Bach, M.; Bertoncel, T.; Meško, M.; Krstić, Ž. Text mining of industry 4.0 job advertisements. *International journal of information management* **2020**, *50*, 416–431.
14. Furstenau, L.B.; Sott, M.K.; Kipper, L.M.; Machado, E.L.; Lopez-Robles, J.R.; Dohan, M.S.; Cobo, M.J.; Zahid, A.; Abbasi, Q.H.; Imran, M.A. Link between sustainability and industry 4.0: trends, challenges and new perspectives. *Ieee Access* **2020**, *8*, 140079–140096.
15. Bag, S.; Gupta, S.; Kumar, S. Industry 4.0 adoption and 10R advance manufacturing capabilities for sustainable development. *International journal of production economics* **2021**, *231*, 107844.

16. Zheng, T.; Ardolino, M.; Bacchetti, A.; Perona, M. The applications of Industry 4.0 technologies in manufacturing context: a systematic literature review. *International Journal of Production Research* **2021**, *59*, 1922–1954.
17. Stentoft, J.; Adsbøll Wickstrøm, K.; Philipsen, K.; Haug, A. Drivers and barriers for Industry 4.0 readiness and practice: empirical evidence from small and medium-sized manufacturers. *Production Planning & Control* **2021**, *32*, 811–828.
18. Meindl, B.; Ayala, N.F.; Mendonça, J.; Frank, A.G. The four smarts of Industry 4.0: Evolution of ten years of research and future perspectives. *Technological Forecasting and Social Change* **2021**, *168*, 120784.
19. Jamwal, A.; Agrawal, R.; Sharma, M.; Giallanza, A. Industry 4.0 technologies for manufacturing sustainability: a systematic review and future research directions. *Applied Sciences* **2021**, *11*, 5725.
20. Atzori, L.; Iera, A.; Morabito, G. The internet of things: A survey. *Computer networks* **2010**, *54*, 2787–2805.
21. Ashton, K.; et al. That 'internet of things' thing. *RFID journal* **2009**, *22*, 97–114.
22. Deering, S.; Hinden, R.; et al. Internet protocol, version 6 (IPv6) specification, 1998.
23. Johnson, D.; Perkins, C.; Arkko, J.; et al. Mobility support in IPv6, 2004.
24. Lee, J.; Bagheri, B.; Kao, H.A. A cyber-physical systems architecture for industry 4.0-based manufacturing systems. *Manufacturing letters* **2015**, *3*, 18–23.
25. Glaessgen, E.; Stargel, D. The digital twin paradigm for future NASA and US Air Force vehicles. In Proceedings of the 53rd AIAA/ASME/ASCE/AHS/ASC structures, structural dynamics and materials conference 20th AIAA/ASME/AHS adaptive structures conference 14th AIAA, 2012, p. 1818.
26. Tuegel, E.J.; Ingraffea, A.R.; Eason, T.G.; Spottswood, S.M. Reengineering aircraft structural life prediction using a digital twin. *International Journal of Aerospace Engineering* **2011**, *2011*.
27. Lee, J.; Lapira, E.; Bagheri, B.; Kao, H.a. Recent advances and trends in predictive manufacturing systems in big data environment. *Manufacturing letters* **2013**, *1*, 38–41.
28. Tao, F.; Qi, Q.; Wang, L.; Nee, A. Digital twins and cyber–physical systems toward smart manufacturing and industry 4.0: Correlation and comparison. *Engineering* **2019**, *5*, 653–661.
29. Jones, D.; Snider, C.; Nassehi, A.; Yon, J.; Hicks, B. Characterising the Digital Twin: A systematic literature review. *CIRP Journal of Manufacturing Science and Technology* **2020**, *29*, 36–52.
30. Errandonea, I.; Beltrán, S.; Arrizabalaga, S. Digital Twin for maintenance: A literature review. *Computers in Industry* **2020**, *123*, 103316.
31. Qi, Q.; Tao, F.; Hu, T.; Anwer, N.; Liu, A.; Wei, Y.; Wang, L.; Nee, A. Enabling technologies and tools for digital twin. *Journal of Manufacturing Systems* **2021**, *58*, 3–21.
32. Rasheed, A.; San, O.; Kvamsdal, T. Digital twin: Values, challenges and enablers from a modeling perspective. *Ieee Access* **2020**, *8*, 21980–22012.
33. Fuller, A.; Fan, Z.; Day, C.; Barlow, C. Digital twin: Enabling technologies, challenges and open research. *IEEE access* **2020**, *8*, 108952–108971.
34. Sacks, R.; Brilakis, I.; Pikas, E.; Xie, H.S.; Girolami, M. Construction with digital twin information systems. *Data-Centric Engineering* **2020**, *1*.
35. VanDerHorn, E.; Mahadevan, S. Digital Twin: Generalization, characterization and implementation. *Decision support systems* **2021**, *145*, 113524.
36. Boje, C.; Guerriero, A.; Kubicki, S.; Rezgui, Y. Towards a semantic Construction Digital Twin: Directions for future research. *Automation in Construction* **2020**, *114*, 103179.
37. Liu, M.; Fang, S.; Dong, H.; Xu, C. Review of digital twin about concepts, technologies, and industrial applications. *Journal of Manufacturing Systems* **2021**, *58*, 346–361.
38. Lim, K.Y.H.; Zheng, P.; Chen, C.H. A state-of-the-art survey of Digital Twin: techniques, engineering product lifecycle management and business innovation perspectives. *Journal of Intelligent Manufacturing* **2020**, *31*, 1313–1337.
39. Kaur, M.J.; Mishra, V.P.; Maheshwari, P. The convergence of digital twin, IoT, and machine learning: transforming data into action. In *Digital twin technologies and smart cities*; Springer, 2020; pp. 3–17.
40. Glatt, M.; Sinnwell, C.; Yi, L.; Donohoe, S.; Ravani, B.; Aurich, J.C. Modeling and implementation of a digital twin of material flows based on physics simulation. *Journal of Manufacturing Systems* **2021**, *58*, 231–245.
41. Lu, Y.; Liu, C.; Kevin, I.; Wang, K.; Huang, H.; Xu, X. Digital Twin-driven smart manufacturing: Connotation, reference model, applications and research issues. *Robotics and Computer-Integrated Manufacturing* **2020**, *61*, 101837.
42. Lu, Q.; Parlikad, A.K.; Woodall, P.; Don Ranasinghe, G.; Xie, X.; Liang, Z.; Konstantinou, E.; Heaton, J.; Schooling, J. Developing a digital twin at building and city levels: Case study of West Cambridge campus. *Journal of Management in Engineering* **2020**, *36*, 05020004.
43. Cimino, C.; Negri, E.; Fumagalli, L. Review of digital twin applications in manufacturing. *Computers in Industry* **2019**, *113*, 103130.
44. Kritzinger, W.; Karner, M.; Traar, G.; Henjes, J.; Sihn, W. Digital Twin in manufacturing: A categorical literature review and classification. *IFAC-PapersOnLine* **2018**, *51*, 1016–1022.
45. He, B.; Bai, K.J. Digital twin-based sustainable intelligent manufacturing: A review. *Advances in Manufacturing* **2021**, *9*, 1–21.
46. Aheleroff, S.; Xu, X.; Zhong, R.Y.; Lu, Y. Digital twin as a service (DTaaS) in industry 4.0: an architecture reference model. *Advanced Engineering Informatics* **2021**, *47*, 101225.

47. Semeraro, C.; Lezoche, M.; Panetto, H.; Dassisti, M. Digital twin paradigm: A systematic literature review. *Computers in Industry* **2021**, *130*, 103469.
48. Singh, M.; Fuenmayor, E.; Hinchy, E.P.; Qiao, Y.; Murray, N.; Devine, D. Digital twin: origin to future. *Applied System Innovation* **2021**, *4*, 36.
49. Wu, Y.; Zhang, K.; Zhang, Y. Digital twin networks: a survey. *IEEE Internet of Things Journal* **2021**, *8*, 13789–13804.
50. Bhatti, G.; Mohan, H.; Singh, R.R. Towards the future of smart electric vehicles: Digital twin technology. *Renewable and Sustainable Energy Reviews* **2021**, *141*, 110801.
51. Negri, E.; Fumagalli, L.; Macchi, M. A review of the roles of digital twin in CPS-based production systems. *Procedia Manufacturing* **2017**, *11*, 939–948.
52. Newmark, N.M. A method of computation for structural dynamics. *Journal of the engineering mechanics division* **1959**, *85*, 67–94.
53. Paz, M. *Structural dynamics: theory and computation*; Springer Science & Business Media, 2012.
54. Soares, R.d.P.; Secchi, A.R. Structural analysis for static and dynamic models. *Mathematical and Computer Modelling* **2012**, *55*, 1051–1067.
55. Guyan, R.J. Reduction of stiffness and mass matrices. *AIAA journal* **1965**, *3*, 380–380.
56. Hurty, W.C. Dynamic analysis of structural systems using component modes. *AIAA journal* **1965**, *3*, 678–685.
57. Craig Jr, R.R.; Bampton, M.C. Coupling of substructures for dynamic analyses. *AIAA journal* **1968**, *6*, 1313–1319.
58. Goldman, R.L. Vibration analysis by dynamic partitioning. *AIAA journal* **1969**, *7*, 1152–1154.
59. Hou, S.; et al. Review of modal synthesis techniques and a new approach. *Shock and vibration bulletin* **1969**, *40*, 25–39.
60. Dowell, E.H. Free vibrations of an arbitrary structure in terms of component modes **1972**.
61. Hintz, R.M. Analytical methods in component modal synthesis. *AIAA Journal* **1975**, *13*, 1007–1016.
62. Benfield, W.; Hruda, R. Vibration analysis of structures by component mode substitution. *AIAA journal* **1971**, *9*, 1255–1261.
63. MacNeal, R.H. A hybrid method of component mode synthesis. *Computers & Structures* **1971**, *1*, 581–601.
64. Rubin, S. Improved component-mode representation for structural dynamic analysis. *AIAA journal* **1975**, *13*, 995–1006.
65. Géradin, M.; Rixen, D.J. *Mechanical vibrations: theory and application to structural dynamics*; John Wiley & Sons, 2014.
66. Lee, H.H. *Finite element simulations with ANSYS Workbench 18*; SDC publications, 2018.
67. Helwany, S. *Applied soil mechanics with ABAQUS applications*; John Wiley & Sons, 2007.
68. MacNeal, R.H. *The NASTRAN theoretical manual*; Vol. 221, Scientific and Technical Information Office, National Aeronautics and Space . . . , 1970.
69. Thomson, W.T. *Theory of vibration with applications*; CrC Press, 2018.
70. Kaszynski, A. pyansys: Python Interface to MAPDL and Associated Binary and ASCII Files, 2020.
71. Ogata, K.; et al. *Modern control engineering*; Vol. 5, Prentice hall Upper Saddle River, NJ, 2010.
72. Stefani, R.T.; Shahian, B.; Savant, C.J.; Hostetter, G.H. *Design of feedback control systems*; Oxford University Press Oxford;, 2002.
73. Nise, N.S. *Control systems engineering*; John Wiley & Sons, 2020.
74. Allemang, R.J.; Brown, D.L. Experimental modal analysis and dynamic component synthesis. volume 3. modal parameter estimation. Technical report, CINCINNATI UNIV OH DEPT OF MECHANICAL AND INDUSTRIAL ENGINEERING, 1987.
75. Kuether, R.J.; Allen, M.S.; Hollkamp, J.J. Modal substructuring of geometrically nonlinear finite element models with interface reduction. *AIAA Journal* **2017**, *55*, 1695–1706.
76. Bulirsch, R.; Stoer, J.; Stoer, J. *Introduction to numerical analysis*; Vol. 3, Springer, 2002.
77. Calvo, M.; Montijano, J.; Randez, L. A fifth-order interpolant for the Dormand and Prince Runge-Kutta method. *Journal of computational and applied mathematics* **1990**, *29*, 91–100.
78. Engstler, C.; Lubich, C. MUR8: a multirate extension of the eighth-order Dormand-Prince method. *Applied numerical mathematics* **1997**, *25*, 185–192.
79. ANSYS, M.A. Advanced analysis guide, 9. *User-programmable features SAS, seventeenth ed., IP Inc* **2016**.
80. ANSYS, M.A. ANSYS Mechanical APDL Theory Reference **2013**.